



Full length article

Flash sintering activated by bulk phase and grain boundary complexion transformations



Yuanyao Zhang, Jiuyuan Nie, Jian Luo*

Department of NanoEngineering, University of California San Diego, La Jolla, CA 92093, USA

ARTICLE INFO

Article history:

Received 30 March 2019

Revised 18 September 2019

Accepted 9 October 2019

Available online 11 October 2019

Keywords:

Flash sintering

Phase transformation

Grain boundary complexion

Field effects

Thermal runaway

ABSTRACT

A naturally-occurring coupled thermal and electric runaway, resulted from an Arrhenius temperature-dependent specimen conductivity, can trigger flash sintering in many ceramics. This study reveals another possibility to activate flash sintering: a bulk phase transformation or a grain boundary (phase-like) complexion transition can cause an abrupt rise in the specimen conductivity to jump start flash sintering (prior to the occurrence of a natural thermal runaway). In undoped and Al₂O₃-doped ZnO, the flash sintering is activated by natural thermal runways that can be quantitatively predicted from an Arrhenius extrapolation of low-temperature specimen conductivity. In contrast, a bulk eutectic reaction and the associated formation of premelting-like intergranular films (IGFs) in Bi₂O₃-doped ZnO can lead to a nonlinear rise in the specimen conductivity (above the Arrhenius extrapolation) to trigger flash sintering prior to the occurrence of the predicted natural thermal runaway. Yet, a natural thermal runaway can still take place in Bi₂O₃-doped ZnO before the occurrence of the interfacial and bulk transformation if the initial electric field is increased to a sufficiently high level. All five cases can be fully explained in a consistent framework so that this set of experiments systematically validate our theory of flash initiation. This work uncovers the roles of the bulk phase and interfacial (phase-like) complexion transformations in initiating flash sintering, thereby suggesting a new direction to understand and tailor the flash sintering process. An observation of ultra-fast field-induced migration of aliovalent cations during the flash sintering of Al₂O₃-doped ZnO is also reported.

© 2019 Acta Materialia Inc. Published by Elsevier Ltd. All rights reserved.

1. Introduction

Flash sintering, a novel sintering technology invented by Raj and coworkers [1,2], has attracted significant scientific and technological interests. Because the densification can occur in seconds at much reduced furnace temperatures, the flash sintering technology has a great potential for significant time, cost, and energy savings. Flash sintering has been applied to various materials, including yttria-stabilized zirconia (YSZ), SiC, BaTiO₃, CeO₂, MgAl₂O₄, and ZnO [3–13]. Fundamental studies have been conducted to probe the cause of the flash initiation [8,14–18], the mechanisms of rapid densification [8,19,20], and the effects of electric fields on phase transformation and microstructural evolution [8,21–26]. Flash sintering is a multi-physics process that involves ultrafast temperature rise (often on the order of 100 °C/s), electric field effects, and far-from-equilibrium rapid microstructure evolution. Thus, a diversifying spectrum of phenomena can occur [8,9,11,24–37].

Sintering aids are often used to promote densification at reduced temperatures in conventional sintering via forming a small amount of liquid phases (in so-called “liquid-phase sintering”) [38–40] or nanoscale premelting like intergranular films (IGFs) (in so-called solid-state “activated sintering” that can occur below the bulk solidus curve) [41–50]. In a broader perspective, recent studies showed that grain boundary complexions (a.k.a. interfacial phases that are thermodynamically two dimensional) [51] can often form and affect the sintering processing (e.g., lowering the onset of sintering via forming premelting like IGFs [41,42,44–46]), microstructural evolution [51–55], and the final mechanical, electrical, and thermal properties [51,56,57]. The possible roles of such grain boundary complexions in flash sintering have been discussed by Todd and co-workers [58] and Harmer and co-workers [52], but have been neither confirmed nor systematically investigated experimentally. This motivated us to dope ZnO with Bi₂O₃, which is known to promote the formation of premelting like IGFs (below the eutectic temperature, T_{eutectic}) and/or a small fraction of a liquid phase (above the T_{eutectic} , still with nanoscale IGFs) to enhance conventional sintering [41,59], to investigate their possible roles in the flash sintering in this study.

* Corresponding author.

E-mail address: jluo@alum.mit.edu (J. Luo).

Several independent studies carried out at UCSD [15], Oxford [14], and U. Penn. [16] collectively demonstrated that natural thermal runaways can trigger flash sintering. Here, we used “natural” thermal runaway to refer to the case where an Arrhenius increasing of the specimen conductivity with increasing temperature triggers a thermal runaway. Furthermore, quantitative models have been developed to show that predicted thermal runaway temperatures are consistent with the observed flash initiation temperatures in a broad range of materials examined [14–16,19,60–62]. Yet, these successes do not rule out the alternative possibilities that, in certain systems, the occurrence of another physical phenomenon, e.g., a bulk phase transformation or an interfacial phase-like (complexion) transformation, can result in a sudden increase in the specimen conductivity to subsequently trigger flash sintering. In such a case, a “forced” (instead of “natural”) thermal runaway will induce the flash sintering. Here, we report, for the first time to our knowledge, such a case in Bi_2O_3 -doped ZnO .

Specifically, this study investigated Bi_2O_3 vs. Al_2O_3 doping effects on the flash sintering of ZnO and revealed that the flash sintering can be more complex than what we previously thought, particularly when it interacts with a bulk phase or an interfacial phase-like transformation. On the one hand, Bi_2O_3 -doping decreased the conductivity of ZnO powder specimens to suppress the natural thermal runaway. Here, we found that the thermal runaway can be triggered indirectly by bulk/interfacial transformations that cause abrupt increase in specimen conductivity (at intermediate and low initial fields) or naturally (at a sufficiently high initial field). On the other hand, Al_2O_3 doping increased the conductivity of ZnO to promote flash sintering via reducing the natural thermal runaway temperature. Here, we further discovered fast field-induced migration of aliovalent $\text{Al}_{\text{Zn}}^{+}$ cations during the flash sintering. Overall, this series of diversifying and scientifically interesting observations, although beyond what had been observed previously, can be fully elucidated within one consistent physics-based theoretical framework.

2. Experimental

ZnO powder (>99.99% purity, Sigma Aldrich) and 0.5 mol% of Bi_2O_3 powder ($\geq 99.8\%$ purity, 90–210 nm particle size; Sigma Aldrich) were mixed in an yttria-stabilized zirconia vial with a small amount of isopropyl alcohol. All powders were subsequently planetary ball milled for 10 h, dried in an oven at 80 °C for 12 h, and calcined at 600 °C for two hours inside an alumina crucible on a Pt foil in air. The 1.6 mol% (1 wt%) Al_2O_3 -doped ZnO powder (99.95% purity, ~15 nm particle size) was purchased from US Research Nanomaterials, Inc.

The powders were uniaxially pressed at ~300 MPa to form a pellet with a dimension of a ¼-inch diameter and ~1-mm thickness. Platinum was sputtered on both sides of the green specimens using a Denton Discovery 18 Sputter. The sides of the sputtered specimens were slightly grounded by SiC papers after sputtering.

Flash sintering experiments were conducted with an initial electric field of 100 V/cm, 300 V/cm, or 800 V/cm, respectively. The applied voltage was kept at constant while ramping the furnace at a constant heating rate of 5 °C per minute until a flash occurred, at which point the system was switched from the voltage-control to a current-control mode with a preset maximum current limit of 1 A (corresponding to the maximum current density of ~39 mA/mm², which limits the steady-state field to ~100 V/cm). Noting that the steady-state field of ~100 V/cm is determined by the preset max current (density) limit and the actual specimen conductivity. The electric power source and furnace were shut down 30 s after the occurrence of the flash. The specimens were cooled with the furnace (and powder supply) being shut down and opened. It takes less than 20 s to safely unload the sample after quenching so that

we estimate the initial cooling rate to be on the order of 100 °C/s. More details about the equipment set up and the experiments can be found in an earlier publication [19].

In addition to monitoring the specimen conductivity (prior to the start of the flash) in all flash sintering experiments, the conductivity of a $\text{ZnO} + 0.5 \text{ mol\% } \text{Bi}_2\text{O}_3$ green specimen was measured in the same equipment setup using a high-precision digital multimeter (Tektronix DMM 4050, Beaverton, OR, USA). The measurement was conducted when the temperature was increased from room temperature to 1200 °C at 5 °C/min (identical to the ramp rate used in the flash sintering experiments) to assess the specimen conductivity in a large temperature range with a high accuracy. For all conductivity measurements, we have subtracted the wire resistances (after measuring the wire resistance vs. temperature in a separate study), and we used thick wires (for less correction errors).

The flash-sintered specimens were characterized by using an ultra-high-resolution scanning electron microscope (UHR SEM, FEI, Hillsboro, OR) equipped with energy dispersive X-ray spectroscopy (EDX, Oxford Instrument, UK). EDX quantitative measurements were taken at cross sections of polished specimens. Each EDX scanned area was set to be $82.4 \times 54.5 \mu\text{m}^2$ at 2500X magnification. All acquisitions reached >500 k full scale counts for better statistical data quality. At each normalized distance to cathode, averaged atomic percentage and corresponding standard deviation were calculated from five independent of measurements. The final averaged atomic percentage was rounded to 0.1 at.% based on the ISO 22309:2011 standard.

Transmission electron microscopy (TEM) specimens were prepared by using a Scios Dual Beam FIB/SEM system (FEI, Hillsboro, OR). High-resolution TEM (HRTEM) characterization of the grain boundary structures was conducted by using a JEOL 2800 microscope operated at 200 kV.

A separate $\text{ZnO} + 0.5 \text{ mol\% } \text{Bi}_2\text{O}_3$ specimen was equilibrated at 700 °C for 24 h in air and subsequently air quenched to room temperature for TEM characterization.

Specifically, HRTEM was used to characterize the liquid-like IGFs formed in both (equilibrated) isothermally-annealed and (presumably non-equilibrium) flash-sintered specimens for comparison.

3. Results and discussion

3.1. Doping effects on the conductivity and flash sintering: Al_2O_3 vs. Bi_2O_3

The measured conductivity (in a logarithmic scale) vs. the reciprocal of the estimated absolute specimen temperature curves for undoped, Bi_2O_3 -doped, and Al_2O_3 -doped ZnO green specimens (i.e., un-sintered but compacted powder pellets; noting that the doped powders had been annealed/homogenized at 600 °C for two hours) are shown in Fig. 1. These conductivity measurements were conducted for the low-temperature regime before sintering would take place. Here, the difference between the specimen and furnace temperatures was estimated by the blackbody radiation model [73].

On the one hand, Al_2O_3 doping increased the conductivity of ZnO (Fig. 1), which is well known (as Al_2O_3 -doped ZnO is a transparent conductor). On the other hand, Bi_2O_3 doping decreased the conductivity of ZnO in this low-temperature region (Fig. 2; noting that the conductivity would increase abruptly near and above the bulk eutectic temperature, which will be discussed later and shown in Fig. 6(a)). A comparison of Fig. 1 and the low-temperature portion of Fig. 6(a) also showed that (1) the measured conductivities of green specimens are independent of the applied voltage and (2) the specimen-to-specimen variations are

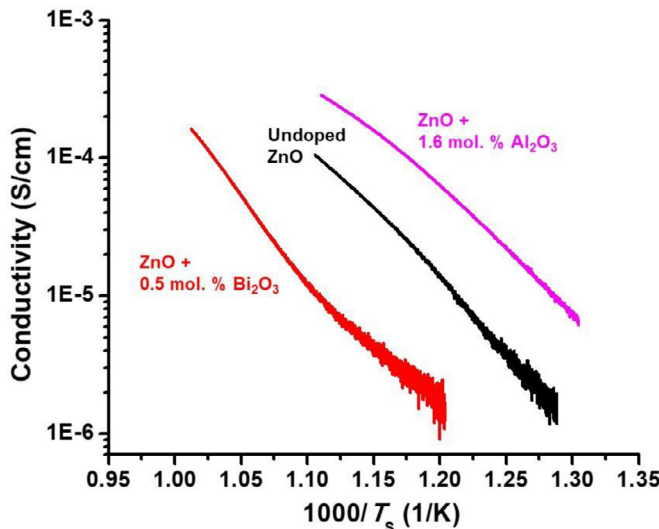


Fig. 1. Logarithmic measured electric conductivity vs. the reciprocal of the absolute specimen temperature curves for undoped, 0.5 mol% Bi_2O_3 -doped, and 1.6 mol% Al_2O_3 -doped ZnO green specimens. (For interpretation of the references to colour in this figure legend, the reader is referred to the web version of this article.)

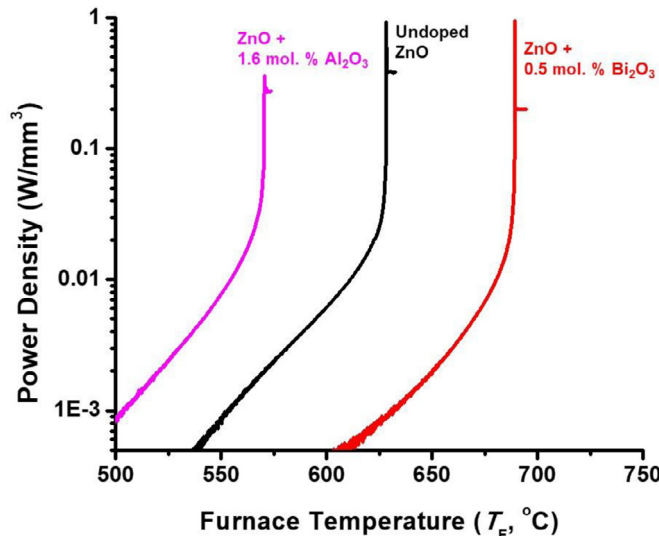


Fig. 2. Measured dissipating electric power density (in a logarithmic scale) vs. furnace temperature curves for the flash sintering of undoped ZnO , 0.5 mol% Bi_2O_3 doped ZnO , and 1.6 mol% Al_2O_3 -doped ZnO (AZO), where the initial electric field was set to be 300 V/cm and the maximum current limit was set to 1 A ($I_{\max} \approx 39 \text{ mA/mm}^2$).

insignificant for these green specimens. Consistently, Al_2O_3 doping promoted, while Bi_2O_3 doping suppressed, the flash sintering, as shown in Fig. 2 and Table 1.

Fig. 2 shows the dissipating electric power density versus furnace temperature in these three specimens, where the initial electric field was set at 300 V/cm and current limit was set at 1 A ($\sim 39 \text{ mA/mm}^2$). The onset flash sintering temperature (furnace T_F) in undoped ZnO was 628 °C; it decreased to ($T_F =$) 570 °C for Al_2O_3 -doped ZnO because of the increased conductivity, while it increased to ($T_F =$) 696 °C for Bi_2O_3 -doped ZnO because of the reduced conductivity (Fig. 2 vs. Fig. 1).

The relative densities of the flash-sintered undoped, Bi_2O_3 -doped, and Al_2O_3 -doped ZnO specimens (with the identical processing parameters of $I_{\max} = 1 \text{ A}$ and $E_{\text{initial}} = 300 \text{ V/cm}$) were measured to be 97.2%, 89.2%, and $\sim 69\%$, respectively. Since the focus here is to examine the doping effects on the flash initiation,

particularly the possible influences of bulk phase transformation and grain boundary phase-like complexion transition, we kept the same flash conditions for undoped, Bi_2O_3 -doped, and Al_2O_3 -doped ZnO for a fair comparison (instead of optimizing the conditions individually for achieving high densities for each case). Consequently, the Al_2O_3 -doped ZnO specimen has a low relative density because the specimen has a significantly higher conductivity in comparison with the other two, thereby resulting in a lower steady-state specimen temperature during flash sintering. By increasing the current limit I_{\max} (from 1 A) to 4 A, however, Al_2O_3 -doped ZnO can also be flash-sintered to $\sim 97\%$ of the theoretical density.

3.2. Undoped and Al_2O_3 -doped ZnO : natural thermal runways

Following our prior procedure [15], the relationship between the temperature-dependent conductivity of the green (compacted powder) specimens was fitted into an empirical Arrhenius equation $\sigma(T) = \sigma_0 e^{-\frac{Q}{kT}}$, where k is the Boltzmann constant, Q is the activation energy, and σ_0 is a pre-exponential constant, for each case. The linear regressions of $\log(\sigma)$ vs. $1/T$ (Fig. 1) for undoped and Al_2O_3 -doped ZnO produced activation energies of 1.02 eV and 1.53 eV, respectively, where the linear correlation coefficients R^2 are higher than 99% in both cases. The $\log(\sigma)$ vs. $1/T$ curve is less linear for the 0.5 mol% Bi_2O_3 -doped ZnO specimen in this temperature region (Fig. 1), where a linear regression gave an R^2 of $\sim 94\%$ with the best fitted activation energy of 1.81 eV. The nonlinearity for the Bi_2O_3 -doped ZnO increases further at higher temperatures, which will be discussed later.

The Arrhenius temperature-dependent conductivity function $\sigma(T)$, which is an extrapolation of the measurements of the unsintered specimen at low temperatures, was subsequently used to predict the thermal runaway condition following a model that we proposed previously [14,15]. Here, a balance between the heat generation from Ohmic (Joule) heating and heat dissipation from blackbody radiation determines the specimen temperature:

$$\sigma(T_S)E^2V_S = A_S\varepsilon\sigma_{\text{Stefan}}(T_S^4 - T_F^4), \quad (1)$$

where E (= E_{initial}) is the electric field, V_S is the volume of the specimen, and T_S and T_F are the specimen (S) and furnace (F) temperatures, respectively, $\sigma(T_S)$ is the specimen conductivity, A_S is the surface area of the specimen, ε is the emissivity, and σ_{Stefan} is the Stefan–Boltzmann constant. A coupled thermal and electric runaway predicted from the Arrhenius extrapolation of the specimen conductivities measured at low temperatures (referred to as a “natural thermal runaway” for brevity hereafter) will take place if there is more heat generated with increasing temperature than that can be dissipated:

$$E^2 \frac{d\sigma}{dT} \Big|_{T_S} \frac{V_S}{A_S} > 4\varepsilon\sigma_{\text{Stefan}}T_S^3, \quad (2)$$

Noting that we divide both sides of Eq. (1) by A_S so that all specimen related parameters are on the left side in Eq. (2).

Eq. (2) suggests a graphical construction method to find the natural thermal runaway condition, as schematically illustrated in Fig. 3. Here, the intersection points of differential heat generation and dissipation rates (both normalized to per unit the specimen surface area, A_S), which are the left and right sides of Eq. (2), determine the specimen temperature (T_S) that produces a natural thermal runaway. Subsequently, the corresponding furnace temperature (T_F) can be calculated based on the blackbody radiation model.

Via this model and the associated graphical construction method (Fig. 3), the furnace temperatures at the natural thermal runways for undoped and Al_2O_3 -doped ZnO specimens ($E_{\text{initial}} = 300 \text{ V/cm}$) were determined to be 628 °C and 564 °C, respectively, using $\sigma(T)$ functions extrapolated from the measured

Table 1

Summary of the key results for the flash sintering of undoped, Al_2O_3 -doped, and Bi_2O_3 -doped ZnO. The thermal runaway conditions were predicted from the Arrhenius extrapolation of the conductivities measured at low temperatures from the (un-sintered) green specimens. The predicted natural thermal runaway conditions are consistent with the experimentally-observed onset flash temperatures for undoped and Al_2O_3 -doped ZnO. For Bi_2O_3 -doped ZnO, the occurrence of a bulk phase (eutectic) transformation and an associated interfacial phase-like (premelting type complexion) transformation can cause a nonlinear rise in the specimen conductivity, thereby triggering a “forced” runaway (prior to the occurrence of a natural thermal runaway) at the initial electric field of 100 or 300 V/cm. At a higher initial field of 800 V/cm, a natural thermal runaway still took place before the occurrence of interfacial and bulk transformation. All observations of five cases can be fully explained within one consistent theoretical framework.

Specimens	Initial electric field $E_{initial}$ (V/cm)	Activation energy for low- T conductivity (eV)	R^2	Predicted thermal runaway specimen $T_S \rightarrow$ estimated furnace T_F		Observed onset flash furnace $T_F \rightarrow$ estimated specimen T_S	The cause for the onset flash	
				T_S (°C)	T_F (°C)			
Un-doped ZnO	300	1.02	> 0.99	777	~628	628	747	Natural thermal runaway
1.6 mol% Al_2O_3 -doped ZnO	300	1.53	> 0.99	610	~564	570	607	Natural thermal runaway
0.5 mol% Bi_2O_3 -doped ZnO	300	1.89	0.94	801	~740	689	~696	GB Transition → Runaway
100	100	1.81	0.9	1005	~960	734	~742	~ Bulk eutectic → Runaway
800	800	1.79	0.99	677	~607	613	~670	Natural thermal runaway

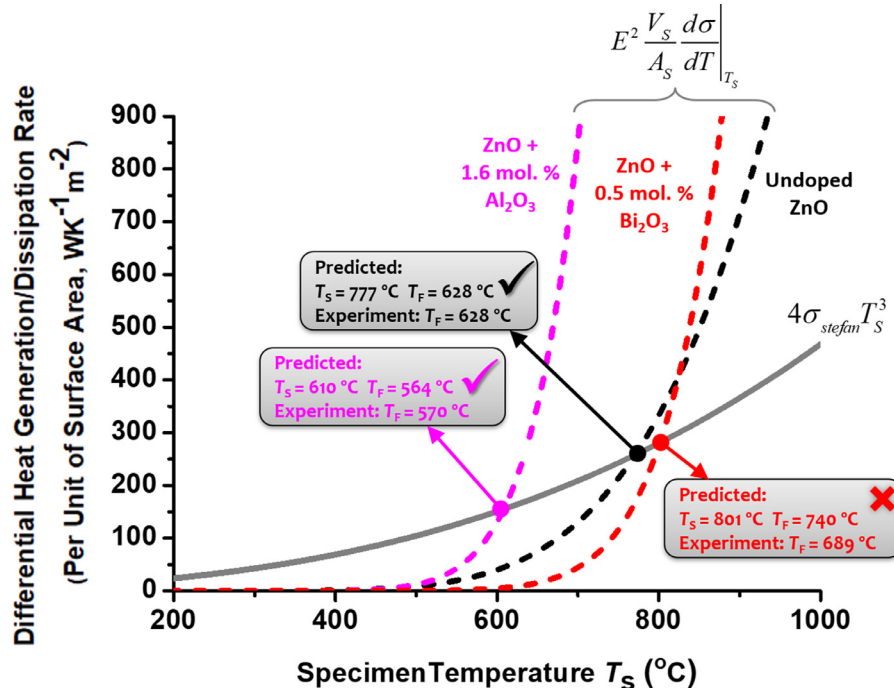


Fig. 3. Calculated differential heat generation and dissipation rates (normalized to per unit surface area) vs. specimen temperature curves for undoped, 0.5 mol% Bi_2O_3 -doped, and 1.6 mol% Al_2O_3 -doped ZnO specimens. The initial electric field was set to be 300 V/cm in each case. The thermal runaway condition can be determined by the intersection of differential heat generation and dissipation rates. The predicted thermal runaway temperatures are consistent with the observed onset flash temperatures for undoped and Al_2O_3 -doped ZnO, but not for the Bi_2O_3 -doped ZnO. A further investigation offers a clear explanation for the apparent discrepancy in the latter case; the natural thermal runaway predicted from the Arrhenius extrapolation of specimen conductivities measured at low temperatures would occur at a specimen temperature of 801 °C for the Bi_2O_3 -doped ZnO; however, a flash actually occurred at a lower specimen temperature near the $\text{ZnO-Bi}_2\text{O}_3$ eutectic temperature of 740 °C, where there was an abrupt increase in the specimen conductivity (beyond the Arrhenius extrapolation) as shown in Fig. 6(a).

conductivities data shown in Fig. 1. Experimentally, we observed onset flash temperatures to be 628 °C for undoped ZnO and 570 °C for Al_2O_3 -doped ZnO, respectively. The differences are small (0 °C and 6 °C, respectively). Thus, we conclude the flash sintering in undoped and Al_2O_3 -doped ZnO specimens was triggered by natural thermal runaways.

For the Bi_2O_3 -doped ZnO specimen at the same $E_{initial} = 300$ V/cm, this model would predict a natural thermal runaway temperature (of $T_F = 740$ °C) from a simple Arrhenius extrapolation of the specimen conductivities measured at low temperatures. However, this predicted natural thermal runaway temperature of $T_F = 740$ °C is 51 °C higher than the observed onset flash temperature (689 °C). This discrepancy is caused by the formation of premelting like IGFs in Bi_2O_3 -doped ZnO, as we will discuss subsequently in Section 3.5.

3.3. Field-driven fast migration of aliovalent cations

Fig. 4 shows the microstructure of the flash-sintered Al_2O_3 -doped ZnO specimen. Notably, aluminum (Al) enriched “white” particles accumulated in the negative electrode (cathode) side (Fig. 4(e)).

Specifically, the enlarged cross-sectional SEM images in Fig. 4(e) vs. Fig. 4(c) reveal “white” particles near the negative electrode (cathode), which are absent in the positive electrode (anode). EDX analyses (Fig. 4(f) vs. Fig. 4(g)) further showed that these “white” particles are Al enriched. The compositions of these white particles were measured to be ~54% O, ~24% Al, and ~22% of Zn. The actual Al content can be even higher considering the possible beam spreading as the particles are sub-micrometer sizes. In comparison, the composition for the normal “dark” particles was measured by

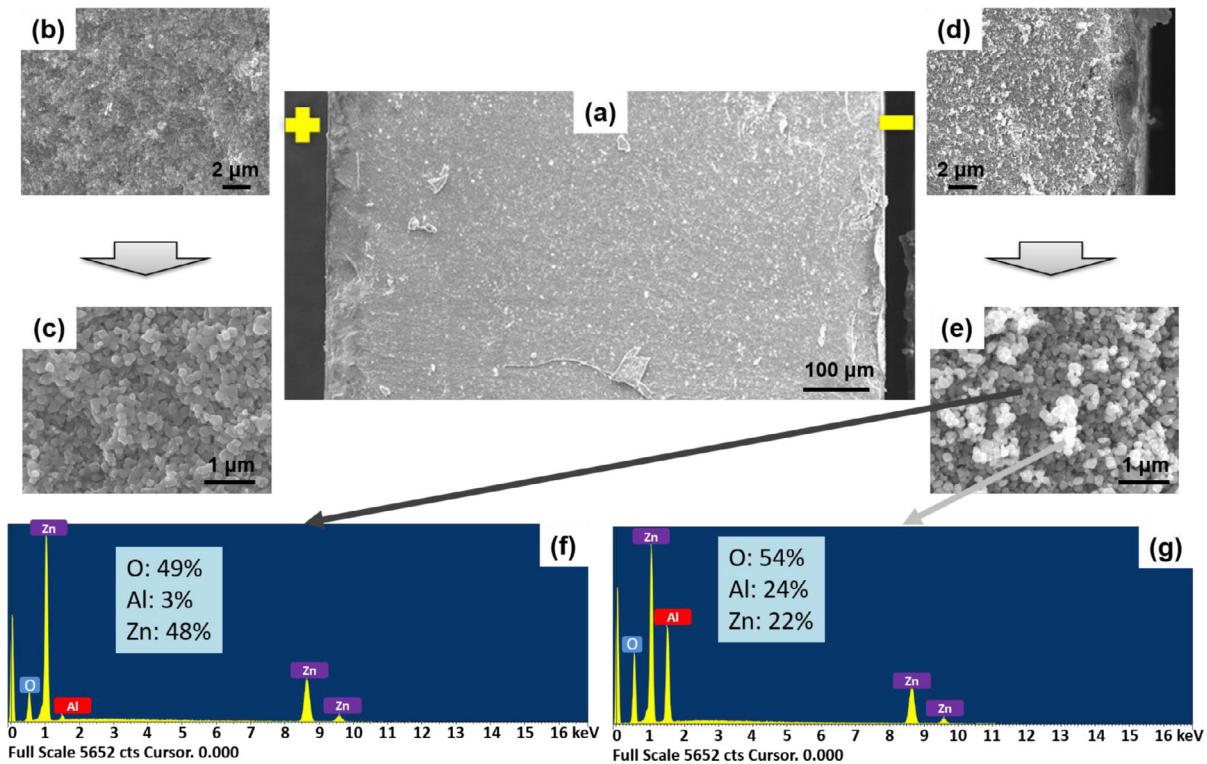


Fig. 4. (a) Cross-sectional SEM image of Al_2O_3 -doped ZnO , along with enlarged SEM images at the (b, c) anode and (d, e) cathode sides. (f, g) EDX quantitative elemental analyses of the “dark particles” and the “white particles”. The compositional analysis clearly showed these “white particles” are Al-enriched. Most “white particles” enriched in Al were observed at the cathode side.

EDX to be ~49% O, ~3% Al, and ~48% Zn, which is close to our nominal powder composition (1.6 mol% Al_2O_3 doped ZnO). Presumably, the white particles are a Zn-Al-O compound, most likely the spinel-structured ZnAl_2O_4 [63], that precipitated during the flash sintering and/or when the specimen was cooled down.

Furthermore, a quantitative SEM EDS analysis was performed on the polished cross section of another flash-sintered Al_2O_3 -doped ZnO specimen. The measured Al percentage (averaged over five individual measurements, each measured from a $82.4 \times 54.5 \mu\text{m}^2$ box for a long collection time to ensure the statistical data accuracies) vs. normalized distance to the cathode is shown in Fig. S1(b) and the data are summarized in Table S1 in the Supplementary Data. It clearly showed that the aluminum concentration is significantly lower near the anode.

The specimen temperature during the steady-state stage of the flash sintering was estimated to be 930 °C. It is known that Al_2O_3 has ~0.3 mol% solubility in ZnO to form charged $\text{Al}_{\text{Zn}}^\bullet$ defects in the temperature range of 850 to 1200 °C [63]. Thus, we hypothesize that the applied electric field/current moved charged $\text{Al}_{\text{Zn}}^\bullet$ defects from the positive to the negative electrode side during the flash sintering, which subsequently precipitated as Al-enriched compound particles upon cooling. Secondary phase particles can be seen in Fig. 4(e) and Supplementary Fig. S1(c). This represents a new discovery of ultrafast, field-driven, asymmetrical microstructural evolution during the flash sintering. It is remarkable that this whole process occurred within ~30 s.

An asymmetrical microstructure was also observed for the flash-sintered 0.5 mol% Bi_2O_3 -doped ZnO sample. Fig. 5 shows the cross-sectional SEM images of flash-sintered Bi_2O_3 -doped ZnO ($E_{\text{initial}} = 300 \text{ V/cm}$). The measured grain size at the negative electrode (cathode) side ($448 \pm 28 \text{ nm}$) approximately doubles that at the positive electrode (anode) side ($212 \pm 16 \text{ nm}$), which suggests a disparity (and therefore a gradient) in microstructural evolution at the cathode and anode sides.

On the one hand, Bi_2O_3 has a much lower solubility in ZnO (< 0.05 mol%), which differs from Al_2O_3 . Thus, the field-driven migration of substitutional aliovalent cations, such as that observed for Al_2O_3 -doped ZnO , was not observed here in Bi_2O_3 -doped ZnO due to the limited solid solubility. On the other hand, it is known that the $\text{ZnO}-\text{Bi}_2\text{O}_3$ solid–liquid two-phase material (above the eutectic temperature) can be used as oxygen ion transport membranes [74], where the intergranular Bi_2O_3 -enriched liquid phase is at least partially an oxygen ionic conductor. The ionic transfer number was measured to be ~0.9 at 840 °C in our experiment (Fig. S2 in the Supplementary Data). The specimen temperature during flash sintering (after the onset of the flash) should be higher so that there should be even more ionic contribution to conductivity. Thus, during the flash sintering of Bi_2O_3 -doped ZnO , the high current density and electric field can induce strong polarization of oxygen defects, which may lead to the different grain sizes at the anode and cathode (Fig. 4). Further investigation should be conducted to probe the detailed underlying mechanism of the observed enhanced grain growth at the cathode side in Bi_2O_3 -doped ZnO .

Yet, we note that the difference between the Bi and Al doping effect is not solely on their different solubility limits (that only affect the well-known electric field driven migration of aliovalent ions). For Bi_2O_3 -doped ZnO , our ongoing study suggests the asymmetric grain growth is related to a GB structural transition, which will be presented and discussed in a separate study.

Electric field induced asymmetric microstructure development has also been observed in SrTiO_3 [65–68], BaTiO_3 [69,70], and Y_2O_3 -stabilized ZrO_2 (YSZ) [71,72], where various mechanisms have been proposed and discussed. In this work, the electric field driven migration of point defect ($\text{Al}_{\text{Zn}}^\bullet$) during flash sintering is no surprise. The underlying mechanism of asymmetric grain growth in Bi_2O_3 -doped ZnO is more subtle, and it will be investigated in-depth in a separate study.

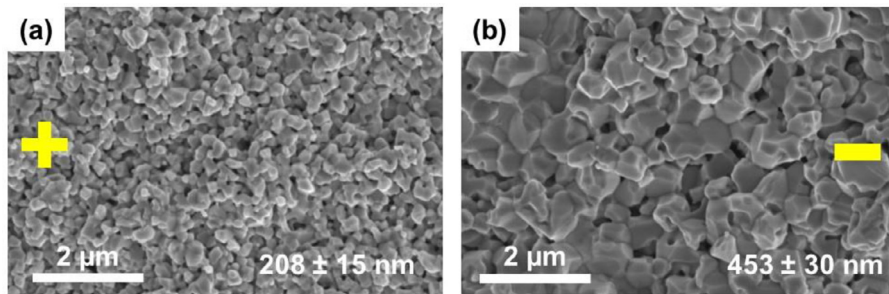


Fig. 5. Cross-sectional SEM images at (a) anode and (b) cathode sides of a flash-sintered Bi_2O_3 -doped ZnO specimen, where the initial electric field (E_{initial}) was set to be 300 V/cm and the maximum current limit was set to 1 A ($J_{\text{max}} \approx 39 \text{ mA/mm}^2$). The grain sizes were measured to be $208 \pm 15 \text{ nm}$ at the anode side and $453 \pm 15 \text{ nm}$ at the cathode side, respectively, suggesting a disparity (thereby a gradient) in the microstructural evolution during the flash sintering.

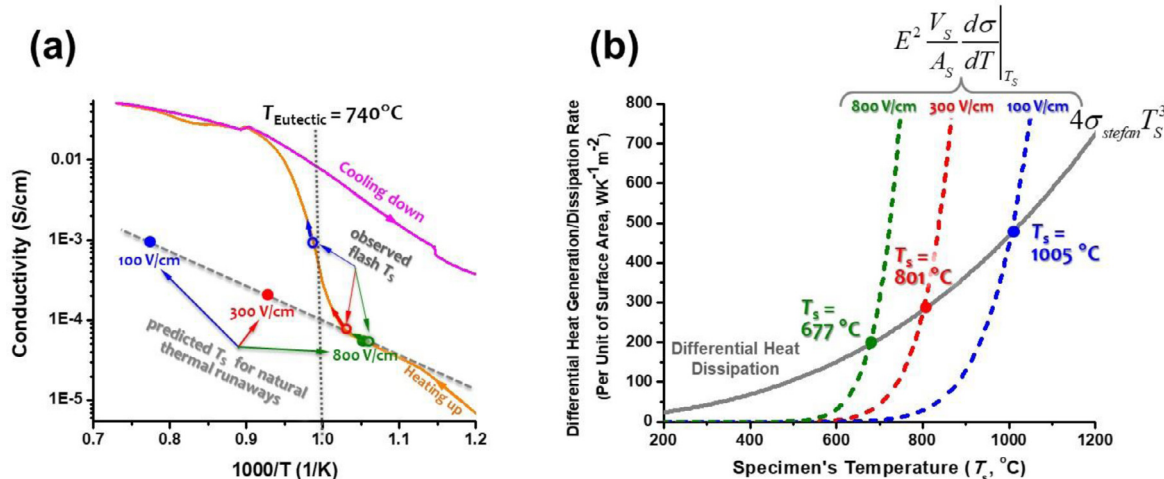


Fig. 6. (a) Measured electric conductivity (in logarithmic scale) vs. the reciprocal absolute specimen temperature curves for a green specimen of $\text{ZnO} + 0.5 \text{ mol\% } \text{Bi}_2\text{O}_3$ heated from room temperature to 1200°C (the orange line) at a ramp rate of $5^\circ\text{C}/\text{min}$, and subsequently cooled down (the pink line). The predicted specimen temperatures (T_S) at natural thermal runaways from the Arrhenius extrapolation from the measured low-temperature conductivities for $E_{\text{initial}} = 100, 300$, and 800 V/cm , respectively, are indicated by the solid discs; the estimated specimen temperatures at the onset flash ("observed flash T_S ") are also marked as open circles with arrows. (b) Calculated differential heat generation and dissipation rates (all normalized to per unit surface area) vs. specimen temperature curves for the flash sintering of $\text{ZnO} + 0.5 \text{ mol\% } \text{Bi}_2\text{O}_3$ specimens with the initial electrical fields of 100, 300, and 800 V/cm , respectively. The thermal runaway conditions predicted from the Arrhenius extrapolations of specimen conductivities measured at low temperatures are determined by the intersections of differential heat generation and dissipation rates. Such predicted thermal runaway temperatures are higher than the experimental observed onset flash temperatures for $E_{\text{initial}} = 100 \text{ V/cm}$ and 300 V/cm because of the nonlinear rise in specimen conductivity near the eutectic temperature. When we further increased E_{initial} to 800 V/cm , the predicted thermal runaway occurred at $T_S \sim 670^\circ\text{C}$, before the nonlinear increase of the specimen conductivity, which agrees with the observed onset flash temperature. (For interpretation of the references to colour in this figure legend, the reader is referred to the web version of this article.)

3.4. Bi_2O_3 -doped ZnO under low E_{initial} : bulk eutectic induced flash

In addition to the natural thermal runaways that can be predicted from the Arrhenius extrapolation of the measured conductivities of the green specimen, here we report a second possibility that the occurrence of a bulk eutectic reaction could trigger flash sintering in $0.5 \text{ mol\% } \text{Bi}_2\text{O}_3$ -doped ZnO via causing a sudden increase in the specimen conductivity (in the eutectic liquid), as a temperature lower than the predicted natural thermal runaway.

Specifically, when a low E_{initial} of 100 V/cm was applied, the specimen temperature for a natural thermal runaway predicted from an Arrhenius extrapolation from the measured conductivities of the green specimen would be 1005°C (Fig. 6(b)). However, flash sintering initiated at the estimated specimen temperature $T_S = 742^\circ\text{C}$ (Fig. 7), which is about the bulk eutectic temperature ($\sim 740^\circ\text{C}$). Presumably, the formation of the Bi_2O_3 -enriched, eutectic liquid caused a sudden increase in the specimen conductivity, thereby triggering the flash sintering via a "forced" thermal runaway.

To confirm the above hypothesis, the electrical conductivity of a $0.5 \text{ mol\% } \text{Bi}_2\text{O}_3$ -doped ZnO specimen was measured when the specimen was heated from room temperature to 1200°C , and sub-

sequently cooled down. The measured $\log(\sigma)$ vs. $1/T$ curves are shown in Fig. 6(a). During the heating, a conductivity transition (i.e., an abrupt increase in measured conductivity) was observed between 690°C and 840°C , which is presumably due to the bulk eutectic reaction (that forms a conducting Bi_2O_3 -based liquid [75]) and associated formation of Bi_2O_3 -enriched, liquid-like, nanoscale IGFs at ZnO grain boundaries (Fig. 8) [41,64]. This is also associated with an increase in ionic transference number, as shown in Fig. S2 in Supplementary Data. During the cooling, the $\log(\sigma)$ vs. $1/T$ curve mostly remained linear (as the Bi_2O_3 -enriched IGFs retained to room temperature). Consistently, the increased ionic transference number also retained after the temperature was reduced from above to below the eutectic temperature (Fig. S2 in Supplementary Data), which is presumably due to the retaining of liquid-like IGFs. The corresponding predicted T_S (for three different E_{initial} 's) from the natural thermal runaway model (Fig. 6(b)) were labeled in Fig. 6(a). These predictions were from the Arrhenius extrapolation (the dash line in Fig. 6(a)) of the conductivities of the green specimen (prior to the occurrence of a conductivity transition). Thus, the natural thermal runaways predicted from the Arrhenius extrapolation did not account for the effect of this conductivity transition.

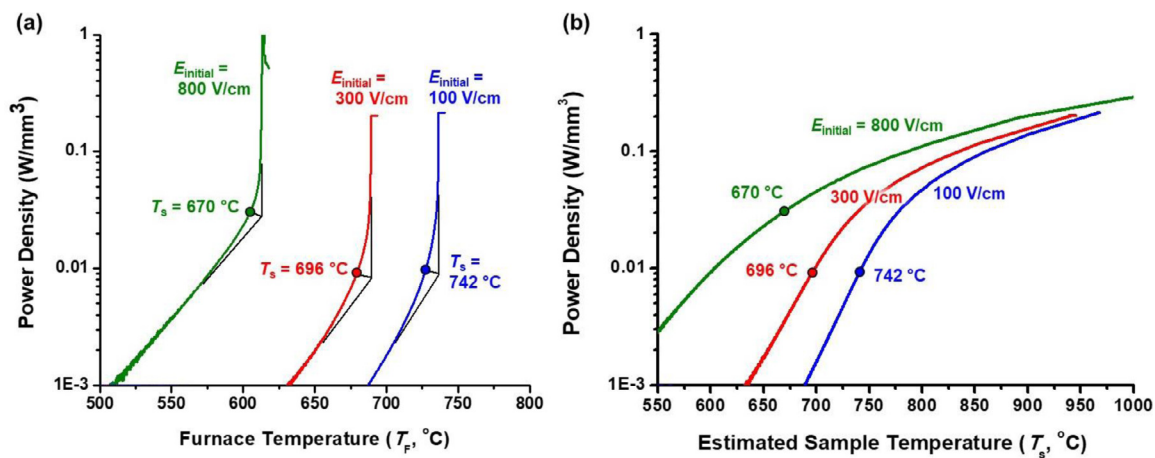


Fig. 7. (a) Measured dissipating electric power density vs. (a) furnace temperature and (b) estimated specimen temperature curves for the flash sintering of 0.5 mol% Bi_2O_3 -doped ZnO specimens, where the initial electric field ($E_{initial}$) was set to be 100, 300, and 800 V/cm, respectively. For each case, the middle point determined by an angular bisector of two tangent lines in panel (a) is considered as the nominal the onset flash point. The corresponding estimated specimen temperatures (T_s) are labeled in both panels as well as Fig. 6(a).

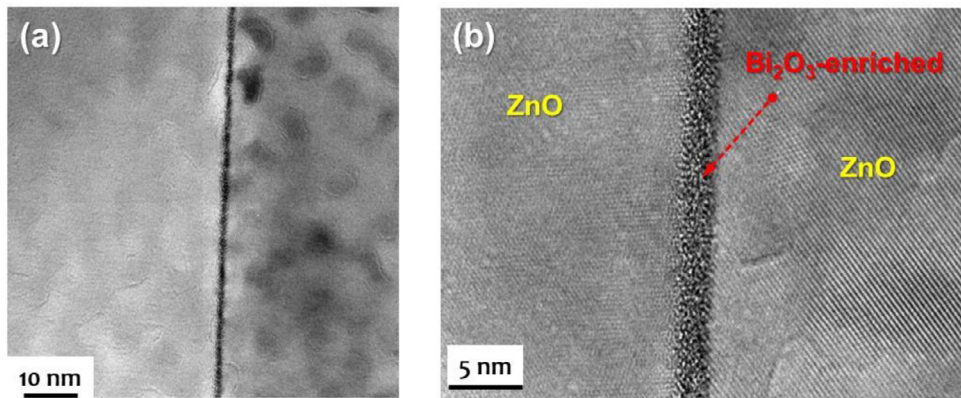


Fig. 8. (a) TEM and (b) HRTEM images of a $\text{ZnO} + 0.5 \text{ mol\% } \text{Bi}_2\text{O}_3$ specimen equilibrated (isothermally annealed) at 700 °C and subsequently air-quenched. A liquid-like Bi_2O_3 -enriched intergranular film (IGF) is stabilized at the ZnO grain boundary below the bulk eutectic temperature ($T_{eutectic} = 740^\circ\text{C}$) where the bulk liquid is not yet stable, which explains the moderate increase of conductivity below the bulk eutectic temperature.

The coincidental occurrences of interface structure change (formation of nanoscale IGFs) and the abrupt increase in the conductivity suggests the increase in conductivity with the temperature is likely caused by the formation of nanoscale IGFs. It is also important to note that here we are talking about the abrupt increase of conductivity with increasing temperature, but not the increase in the conductivity with Bi_2O_3 doping. In fact, Bi_2O_3 -doping reduces the conductivity at low temperatures, as shown in Fig. 1.

Specifically, ionic transference numbers were measured for a Bi_2O_3 -doped ZnO green specimen (a powder pellet) at 600 °C, 680 °C, and 780 °C sequentially during heating (at 5 °C/m), and subsequently cooling (at -5 °C/m) to 600 °C, and the results are shown in Fig. S2 in the Supplementary Data. Together with the measured total conductivity vs. temperature shown in Fig. 7(a), we found the following:

- Below the eutectic temperature (740 °C), the ionic transference number was measured to be ~0.25 at 600 °C and ~0.22 at 680 °C, respectively.
- It increased ~0.38 above the eutectic temperature at 780 °C, presumably due to the formation of liquid IGFs (Fig. 9). Here, we note that the total conductivity also increased with increasing temperature, with an abrupt increase around the eutectic temperature, as shown in Fig. 7(a).

• When the same specimen was cooled (from above the eutectic temperature) back 600 °C (below the eutectic temperature, 740 °C), the ionic transference number remained at (in fact slightly increased to) ~0.38, presumably due to the remaining of liquid-like IGFs.

In summary, the conductivity is largely electronic at the onset of flash with increasing ionic contribution with increasing (onset flash) temperature due to the formation a Bi_2O_3 -based secondary liquid phase and liquid-like IGFs. However, our phenomenological model for predicting the onset flash temperature applies regardless of the nature of the conductivity. The conductivity likely became most ionic after the flash when the specimen temperature is higher. The ionic transference number was measured to be ~0.9 from another pre-sintered specimen after annealing at 840 °C, and it should be even higher at the estimated specimen temperature of 840 °C in the steady state after the flash initiation.

We should further note that conductivity shown in Fig. 6(a), as well as the ionic transference numbers, was measured during furnace heating (at 5 °C/min) and the actual conductivity transition profile should also depend on the heating rate, which was much faster in the flash sintering and could also depend on $E_{initial}$.

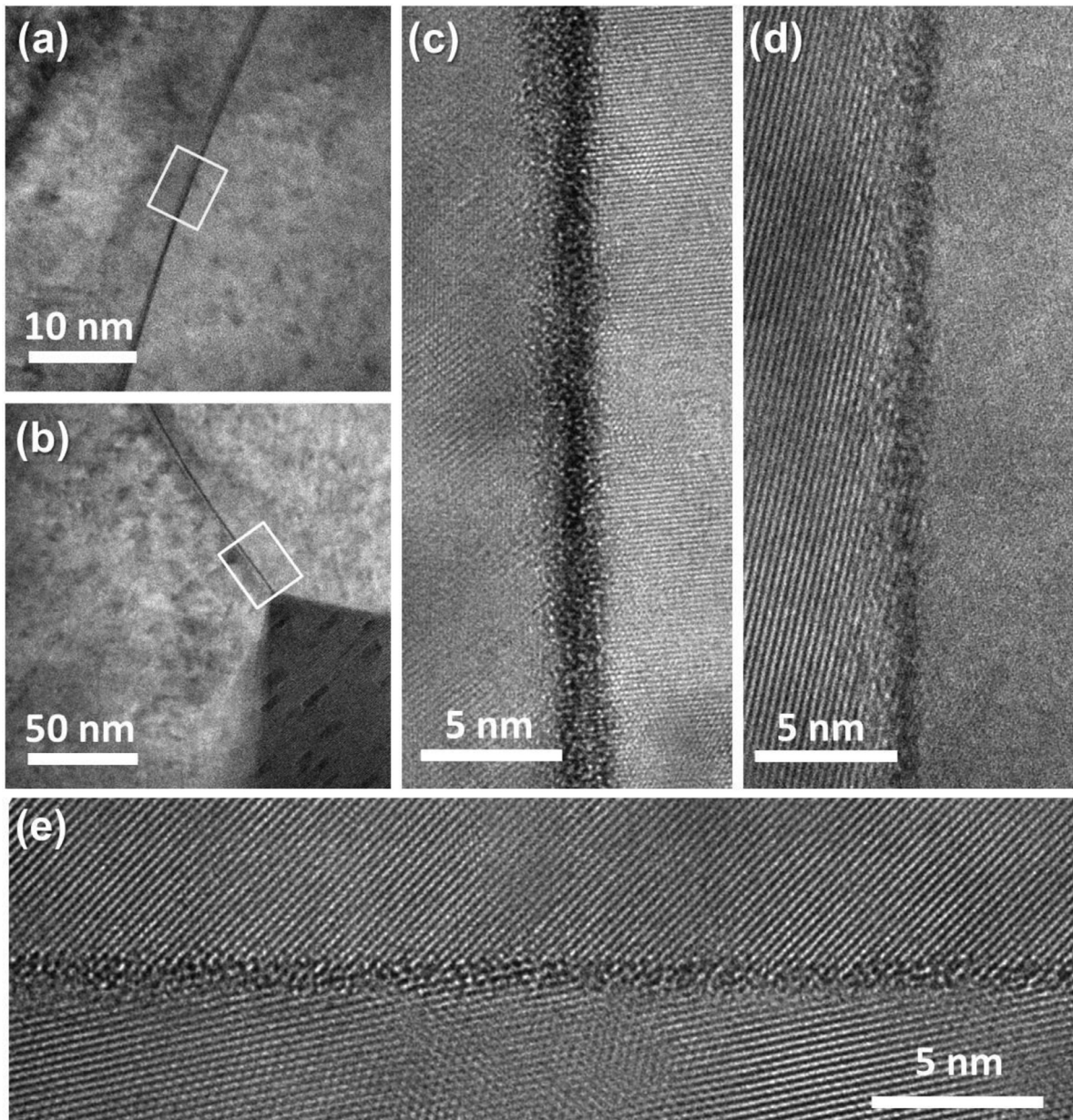


Fig. 9. (a, b) Low- and (c, d, e) high-magnification TEM images of a $\text{ZnO} + 0.5 \text{ mol\% Bi}_2\text{O}_3$ specimen after flash sintering for 20 s, where the initial electric field (E_{initial}) was set to be 300 V/cm and the maximum current limit was set to 1 A ($J_{\text{max}} \approx 39 \text{ mA/mm}^2$). HRTEM images (c) and (d), respectively, correspond to the locations labeled in low-magnification TEM images (a) and (b), respectively.

Upon cooling, the liquid-like IGFs remained in the specimen with enhanced conductivity (Fig. 7a) and ionic transference number (Supplementary Fig. S2) being retained. However, its temperature dependence exhibits a slightly different activation energy as shown in Fig. 6(a), which may represent a grain boundary glass-like transition.

When a low E_{initial} of 100 V/cm was applied, the specimen experienced a significant increase of conductivity (~10 times higher above the Arrhenius extrapolation) before the onset of flash at $T_S = 742^\circ\text{C}$, which triggered a “forced” thermal runaway that is $> 250^\circ\text{C}$ lower than predicted T_S for a natural thermal runaway (from an Arrhenius extrapolation). Thus, the experimental observation (and the discrepancy between the onset flash and the natural thermal runaway predicted from an Arrhenius extrapolation) can be fully explained. In this case, the bulk eutectic reaction at $\sim 740^\circ\text{C}$ triggered a “forced” thermal runaway, and a flash event thereafter, via forming a conducting, Bi_2O_3 -enriched, ionic liquid.

3.5. Bi_2O_3 -doped ZnO under intermediate E_{initial} : interfacial transition induced flash

Moreover, we observed that further increasing E_{initial} initiated flash sintering at a sub-eutectic specimen temperature. When E_{initial} was 300 V/cm, the estimated T_S for onset flash in the experiment was 696°C (Fig. 7(a)); noting the stability is lost at $> 696^\circ\text{C}$ as shown in Fig. 7(a), coincident with a sudden rise in the specimen conductivity as shown in Fig. 6(a). This observed onset flash specimen temperature is $> 40^\circ\text{C}$ lower than the bulk eutectic temperature, but the specimen conductivity started to increase substantially beyond the linear Arrhenius extrapolation line at this temperature as shown in Fig. 6(a); here, we should note 696°C is the nominal specimen temperature for the onset flash, which is defined as the middle point in Fig. 7(a); the actual onset flash occurred in a short time period where the specimen temperature further increased beyond the middle point of $T_S = 696^\circ\text{C}$, after

which the specimen temperature increased abruptly as shown in Fig. 6(a), before losing the stability to trigger the flash sintering. This was presumably resulted from the enhanced interfacial conductivity in the nanometer-thick, Bi_2O_3 -based, liquid-like IGFs that can form below the bulk eutectic temperature [41] (i.e., a premelting like complexion thermodynamically stabilized at ZnO grain boundaries).

It is interesting to note that this moderate increase in the interfacial conductivity of the specimen was insufficient to trigger a flash at the low $E_{initial}$ of 100 V/cm, but it became significant when $E_{initial}$ was increased to 300 V/cm. Presumably, a higher $E_{initial}$ requires a less significant non-linear increase in the specimen conductivity to trigger flash sintering via a “forced” thermal runaway. This is consistent with that the predicted T_s for a natural thermal runaway was 801 °C at 300 V/cm, much lower than the 1005 °C at 100 V/cm (Fig. 6(b)). Experimentally, we observed that the flash sintering initiated at 742 °C (approximately the bulk eutectic temperature) at the low $E_{initial}$ of 100 V/cm, but at a sub-eutectic temperature (696 °C) at the median $E_{initial}$ of 300 V/cm (Fig. 7).

To confirm the above hypothesis directly, we conducted further experiments to directly characterize the grain boundary structures responsible for the increased interfacial conductivity below bulk eutectic temperature in two types of specimens, which are discussed below.

First, a 0.5 mol% Bi_2O_3 -doped ZnO specimen was isothermally annealed at 700 °C (40 °C below the bulk eutectic temperature) and air-quenched to preserve the grain boundary structures. Fig. 8(b) shows TEM and HRTEM images of Bi-enriched, liquid-like IGFs that are stabilized at ZnO grain boundaries, even below the bulk eutectic temperature. The IGFs formed in the specimen equilibrated at 700 °C were measured to be ~2 nm thick in this study. Prior studies already showed that the formation of such sub-eutectic, premelting like IGFs can enhance sintering [41,45]. In this study, the formation of these Bi_2O_3 -enriched, liquid-like, nanoscale IGFs presumably increased the interfacial conductivity below the bulk $T_{eutectic}$ to trigger the flash sintering under the intermediate $E_{initial}$ of 300 V/cm.

Second, we further confirmed the ultra-fast formation of liquid-like IGFs during flash sintering directly. Specifically, we quenched a 0.5 mol% Bi_2O_3 -doped ZnO specimen after being flash sintered for 20 s. Fig. 9 shows two low-magnification and three high-magnification TEM images of the grain boundaries in this flash-sintered specimen. The liquid-like IGFs observed in the flash-sintered specimen are relatively thinner than those observed in the specimen equilibrated at 700 °C. Presumably, these liquid-like IGFs did not form at a thermodynamic equilibrium due to the ultrafast flash sintering process. Nonetheless, this result directly confirmed that such liquid-like IGFs could form quickly (in <20 s) during the flash sintering. Whether such IGFs can form within seconds is unknown (controversial) in prior studies of conventional sintering. Thus, this ultra-fast formation of liquid-like IGFs is a useful result.

3.6. Bi_2O_3 -doped ZnO under high $E_{initial}$: a natural thermal runaway

If the above explanations and hypotheses (discussed in Sections 3.4 and 3.5) are correct, we should be able to further increase $E_{initial}$ to allow the occurrence of a natural thermal runaway prior to the bulk eutectic reaction and interfacial premelting like transition. Indeed, we were able to confirm this prediction by our experiment. When we further increased $E_{initial}$ to 800 V/cm, our model predicted a natural thermal runaway at a specimen temperature $T_s = 677$ °C (>70 °C below the bulk eutectic temperature), as shown in Fig. 6(b). Indeed, we observed that the onset flash took place at an estimated specimen T_s of 670 °C (for a specimen of the same composition of 0.5 mol.% Bi_2O_3 -doped ZnO) in our experiment (Fig. 7).

This agreement is the final case to confirm that the experimental observations of all five cases (un-doped and Al_2O_3 -doped ZnO at $E_{initial} = 300$ V/cm, as well as Bi_2O_3 -doped ZnO at $E_{initial} = 100$, 300, and 800 V/cm, respectively) can be fully explained within one consistent theoretical framework.

4. Conclusions

We investigated Al_2O_3 vs. Bi_2O_3 doping effects on the flash sintering of ZnO . On the one hand, Al_2O_3 doping increased the specimen conductivity to promote flash sintering. The onset flash occurred as natural thermal runaway in both un-doped and Al_2O_3 -doped ZnO at $E_{initial}$ of 300 V/cm.

We also observed ultrafast field-induced migration of aliovalent cations during the flash sintering of Al_2O_3 -doped ZnO .

On the other hand, Bi_2O_3 doping decreased the specimen conductivity to delay the occurrence of flash sintering to higher temperatures, while it also led to a eutectic reaction and associated premelting-like grain boundary transition that can abruptly increase the specimen conductivity with increasing temperature. Consequently, the onset flash was initiated by a bulk eutectic reaction at a low $E_{initial}$ of 100 V/cm and by premelting like grain boundary transition at an intermediate $E_{initial}$ of 300 V/cm, respectively, in 0.5 mol% Bi_2O_3 -doped ZnO . When we further increased $E_{initial}$ to 800 V/cm, a natural thermal runaway still took place before the occurrence of interfacial and bulk transformation, as predicted by the Arrhenius extrapolation.

Notably, we demonstrated that all five cases discussed above can be fully explained within one consistent theoretical framework.

This study has uncovered, for the first time to our knowledge, the possibility that a bulk phase transformation and/or interfacial (phase-like) complexion transformation can trigger flash sintering (via “forced,” instead of natural, thermal runaway). This new discovery thus suggests a new direction to tailor the flash sintering process.

Declaration of Competing Interest

The authors declare that they have no known competing financial interests or personal relationships that could have appeared to influence the work reported in this paper.

Acknowledgment

This work is supported by the Aerospace Materials for Extreme Environments program of the U.S. Air Force Office of Scientific Research (AFOSR) under award numbers FA9550-14-1-0174 (2014–2019) and FA9550-19-1-0327 (2019–2022). We thank our AFOSR program manager, Dr. Ali Sayir, for his support and guidance.

Supplementary materials

Supplementary material associated with this article can be found, in the online version, at doi:[10.1016/j.actamat.2019.10.009](https://doi.org/10.1016/j.actamat.2019.10.009).

References

- [1] M. Cologna, B. Rashkova, R. Raj, Flash sintering of nanograin zirconia in < 5 s at 850 °C, J. Am. Ceram. Soc. 93 (11) (2010) 3556–3559.
- [2] M. Cologna, A.L. Prette, R. Raj, Flash-sintering of cubic yttria-stabilized zirconia at 750 °C for possible use in SOFC manufacturing, J. Am. Ceram. Soc. 94 (2) (2011) 316–319.
- [3] M. Cologna, A.L.G. Prette, R. Raj, Flash-Sintering of cubic yttria-stabilized zirconia at 750 °C for possible use in SOFC manufacturing, J. Am. Ceram. Soc. 94 (2) (2011) 316–319.
- [4] E. Zapata-Solvias, S. Bonilla, P.R. Wilshaw, R.I. Todd, Preliminary investigation of flash sintering of SiC, J. Eur. Ceram. Soc. 33 (13–14) (2013) 2811–2816.

- [5] X.M. Hao, Y.J. Liu, Z.H. Wang, J.S. Qiao, K.N. Sun, A novel sintering method to obtain fully dense gadolinia doped ceria by applying a direct current, *J. Power Sources* 210 (2012) 86–91.
- [6] R. Muccillo, E.N.S. Muccillo, M. Kleitz, Densification and enhancement of the grain boundary conductivity of gadolinium-doped barium cerate by ultra fast flash grain welding, *J. Eur. Ceram. Soc.* 32 (10) (2012) 2311–2316.
- [7] C. Schmerbauch, J. Gonzalez-Julian, R. Roder, C. Ronning, O. Guillou, Flash sintering of nanocrystalline zinc oxide and its influence on microstructure and defect formation, *J. Am. Ceram. Soc.* 97 (6) (2014) 1728–1735.
- [8] J. Luo, The scientific questions and technological opportunities of flash sintering: from a case study of ZnO to other ceramics, *Scr. Mater.* 146 (2018) 260–266.
- [9] M. Yu, S. Grasso, R. McKinnon, T. Saunders, M.J. Reece, Review of flash sintering: materials, mechanisms and modelling, *Adv. Appl. Ceram.* 116 (1) (2017) 24–60.
- [10] M. Biesuz, V.M. Sglavo, Flash sintering of ceramics, *J. Eur. Ceram. Soc.* 39 (2–3) (2019) 115–143.
- [11] R. Todd, Flash sintering of ceramics: a short review, in: Proceedings of the IV Advanced Ceramics and Applications Conference, Springer, 2017, pp. 1–12.
- [12] B. Yoon, D. Yadav, S. Ghose, R. Raj, Reactive flash sintering: MgO and $\alpha\text{-Al}_2\text{O}_3$ transform and sinter into single-phase polycrystals of MgAl_2O_4 , *J. Am. Ceram. Soc.* 102 (5) (2019) 2294–2303.
- [13] X. Vendrell, D. Yadav, R. Raj, A.R. West, Influence of flash sintering on the ionic conductivity of 8 mol% yttria stabilized zirconia, *J. Eur. Ceram. Soc.* 39 (4) (2019) 1352–1358.
- [14] R.I. Todd, E. Zapata-Solvas, R.S. Bonilla, T. Sneddon, P.R. Wilshaw, Electrical characteristics of flash sintering: thermal runaway of joule heating, *J. Eur. Ceram. Soc.* 35 (6) (2015) 1865–1877.
- [15] Y. Zhang, J.I. Jung, J. Luo, Thermal runaway, flash sintering and asymmetrical microstructural development of ZnO and ZnO-Bi₂O₃ under direct currents, *Acta Mater.* 94 (2015) 87–100.
- [16] Y.H. Dong, I.W. Chen, Onset criterion for flash sintering, *J. Am. Ceram. Soc.* 98 (12) (2015) 3624–3627.
- [17] J.G.P. da Silva, H.A. Al-Qureshi, F. Keil, R. Janssen, A dynamic bifurcation criterion for thermal runaway during the flash sintering of ceramics, *J. Eur. Ceram. Soc.* 36 (5) (2016) 1261–1267.
- [18] Y.Y. Zhang, J.Y. Nie, J. Luo, Effects of phase and doping on flash sintering of TiO₂, *J. Ceram. Soc. Jpn.* 124 (4) (2016) 296–300.
- [19] Y.Y. Zhang, J.Y. Nie, J.M. Chan, J. Luo, Probing the densification mechanisms during flash sintering of ZnO, *Acta Mater.* 125 (2017) 465–475.
- [20] W. Ji, B. Parker, S. Falco, J.Y. Zhang, Z.Y. Fu, R.I. Todd, Ultra-fast firing: effect of heating rate on sintering of 3YSZ, with and without an electric field, *J. Eur. Ceram. Soc.* 37 (6) (2017) 2547–2551.
- [21] S.K. Jha, J.M. Lebrun, R. Raj, Phase transformation in the alumina-titania system during flash sintering experiments, *J. Eur. Ceram. Soc.* 36 (3) (2016) 733–739.
- [22] Y. Zhang, J. Luo, Promoting the flash sintering of ZnO in reduced atmospheres to achieve nearly full densities at furnace temperatures of < 120 °C, *Scr. Mater.* 106 (2015) 26–29.
- [23] J.M. Lebrun, R. Raj, A first report of photoemission in experiments related to flash sintering, *J. Am. Ceram. Soc.* 97 (8) (2014) 2427–2430.
- [24] B. Yoon, D. Yadav, R. Raj, E.P. Sortino, S. Ghose, P. Sarin, D. Shoemaker, Measurement of O and Ti atom displacements in TiO₂ during flash sintering experiments, *J. Am. Ceram. Soc.* 101 (5) (2018) 1811–1817.
- [25] D. Kok, D. Yadav, E. Sortino, S.J. McCormack, K.P. Tseng, W.M. Kriven, R. Raj, M.L. Mecartney, α -Alumina and spinel react into single-phase high-alumina spinel in < 3 s during flash sintering, *J. Am. Ceram. Soc.* 102 (2) (2019) 644–653.
- [26] S.K. Jha, X.L. Phuah, J. Luo, C.P. Grigoropoulos, H. Wang, E. García, B. Reejayyan, The effects of external fields in ceramic sintering, *J. Am. Ceram. Soc.* 102 (1) (2019) 5–31.
- [27] J.M. Lebrun, C.S. Hellberg, S.K. Jha, W.M. Kriven, A. Steveson, K.C. Seymour, N. Bernstein, S.C. Erwin, R. Raj, In-situ measurements of lattice expansion related to defect generation during flash sintering, *J. Am. Ceram. Soc.* 100 (11) (2017) 4965–4970.
- [28] R. Raj, Analysis of the power density at the onset of flash sintering, *J. Am. Ceram. Soc.* 99 (10) (2016) 3226–3232.
- [29] K. Naik, S.K. Jha, R. Raj, Correlations between conductivity, electroluminescence and flash sintering, *Scr. Mater.* 118 (2016) 1–4.
- [30] C.E.J. Dancer, Flash sintering of ceramic materials, *Mater. Res. Express* 3 (10) (2016) 102001.
- [31] L.B. Caliman, R. Bouchet, D. Gouvea, P. Soudant, M.C. Steil, Flash sintering of ionic conductors: the need of a reversible electrochemical reaction, *J. Eur. Ceram. Soc.* 36 (5) (2016) 1253–1260.
- [32] C. McLaren, W. Heffner, R. Tessarollo, R. Raj, H. Jain, Electric field-induced softening of alkali silicate glasses, *Appl. Phys. Lett.* 107 (18) (2015) 184101.
- [33] J.-M. Lebrun, T.G. Morrissey, J.S.C. Francis, K.C. Seymour, W.M. Kriven, R. Raj, Emergence and extinction of a new phase during on-off experiments related to flash sintering of 3YSZ, *J. Am. Ceram. Soc.* 98 (5) (2015) 1493–1497.
- [34] K.S. Naik, V.M. Sglavo, R. Raj, Flash sintering as a nucleation phenomenon and a model thereof, *J. Eur. Ceram. Soc.* 34 (15) (2014) 4063–4067.
- [35] J.-M. Lebrun, R. Raj, A first report of photoemission in experiments related to flash sintering, *J. Am. Ceram. Soc.* 97 (8) (2014) 2427–2430.
- [36] P. Kumar MK, D. Yadav, J.M. Lebrun, R. Raj, Flash sintering with current rate: a different approach, *J. Am. Ceram. Soc.* 102 (2) (2019) 823–835.
- [37] W. Rheinheimer, X.L. Phuah, H. Wang, F. Lemke, M.J. Hoffmann, H. Wang, The role of point defects and defect gradients in flash sintering of perovskite oxides, *Acta Mater.* 165 (2019) 398–408.
- [38] W.D. Kingery, Densification during sintering in the presence of a liquid phase. I. Theory, *J. Appl. Phys.* 30 (3) (1959) 301–306.
- [39] W.D. Kingery, M.D. Narasimhan, Densification during sintering in the presence of a liquid phase. 2. Experimental, *J. Appl. Phys.* 30 (3) (1959) 307–310.
- [40] R. German, P. Suri, S. Park, Review: liquid phase sintering, *J. Mater. Sci.* 44 (1) (2009) 1–39.
- [41] J. Luo, H.F. Wang, Y.M. Chiang, Origin of solid-state activated sintering in Bi₂O₃-doped ZnO, *J. Am. Ceram. Soc.* 82 (4) (1999) 916–920.
- [42] V.K. Gupta, D.H. Yoon, H.M. Meyer, J. Luo, Thin intergranular films and solid-state activated sintering in nickel-doped tungsten, *Acta Mater.* 55 (9) (2007) 3131–3142.
- [43] J.L. Johnson, R.M. German, Theoretical modeling of densification during activated solid-state sintering, *Metall. Mater. Trans. A – Phys. Metall. Mater. Sci.* 27 (2) (1996) 441–450.
- [44] J.Y. Nie, J.M. Chan, M.D. Qin, N.X. Zhou, J.A. Luo, Liquid-like grain boundary complexion and sub-eutectic activated sintering in CuO-doped TiO₂, *Acta Mater.* 130 (2017) 329–338.
- [45] J. Luo, Developing interfacial phase diagrams for applications in activated sintering and beyond: current status and future directions, *J. Am. Ceram. Soc.* 95 (8) (2012) 2358–2371.
- [46] X.M. Shi, J. Luo, Developing grain boundary diagrams as a materials science tool: a case study of nickel-doped molybdenum, *Phys. Rev. B* 84 (1) (2011) 14.
- [47] N. Zhou, J. Luo, Developing grain boundary diagrams for multicomponent alloys, *Acta Mater.* 91 (2015) 202–216.
- [48] X. Shi, J. Luo, Grain boundary wetting and prewetting in Ni-doped Mo, *Appl. Phys. Lett.* 94 (25) (2009) 251908.
- [49] J. Luo, X. Shi, Grain boundary disordering in binary alloys, *Appl. Phys. Lett.* 92 (10) (2008) 101901.
- [50] J. Luo, V. Gupta, D. Yoon, H. Meyer III, Segregation-induced grain boundary premelting in nickel-doped tungsten, *Appl. Phys. Lett.* 87 (23) (2005) 231902.
- [51] P.R. Cantwell, M. Tang, S.J. Dillon, J. Luo, G.S. Rohrer, M.P. Harmer, Overview no. 152: grain boundary complexions, *Acta Mater.* 62 (2014) 1–48.
- [52] A.R. Krause, P.R. Cantwell, C.J. Marvel, C. Compson, J.M. Rickman, M.P. Harmer, Review of grain boundary complexion engineering: know your boundaries, *J. Am. Ceram. Soc.* 102 (2) (2019) 778–800.
- [53] S.J. Dillon, M.P. Harmer, Demystifying the role of sintering additives with “complexion”, *J. Eur. Ceram. Soc.* 28 (7) (2008) 1485–1493.
- [54] S.J. Dillon, M. Tang, W.C. Carter, M.P. Harmer, Complexion: a new concept for kinetic engineering in materials science, *Acta Mater.* 55 (18) (2007) 6208–6218.
- [55] S.J. Dillon, M.P. Harmer, Multiple grain boundary transitions in ceramics: a case study of alumina, *Acta Mater.* 55 (2007) 5247–5254.
- [56] J. Luo, Stabilization of nanoscale quasi-liquid interfacial films in inorganic materials: a review and critical assessment, *Crit. Rev. Solid State Mater. Sci.* 32 (1–2) (2007) 67–109.
- [57] W.D. Kaplan, D. Chatain, P. Wynblatt, W.C. Carter, A review of wetting versus adsorption, complexions, and related phenomena: the rosetta stone of wetting, *J. Mater. Sci.* 48 (2013) 5681–5717.
- [58] J.Y. Zhang, F.C. Meng, R.I. Todd, Z.Y. Fu, The nature of grain boundaries in alumina fabricated by fast sintering, *Scr. Mater.* 62 (9) (2010) 658–661.
- [59] X.M. Shi, J. Luo, Developing grain boundary diagrams as a materials science tool: a case study of nickel-doped molybdenum, *Phys. Rev. B* 84 (1) (2011).
- [60] Y.H. Dong, I.W. Chen, Predicting the onset of flash sintering, *J. Am. Ceram. Soc.* 98 (8) (2015) 2333–2335.
- [61] Y. Zhang, J. Nie, J. Luo, Effects of phase and doping on flash sintering of TiO₂, *J. Ceram. Soc. Jpn.* 124 (4) (2016) 296–300.
- [62] Y. Zhang, J. Luo, Promoting the flash sintering of ZnO in reduced atmospheres to achieve nearly full densities at furnace temperatures of <120°C, *Scr. Mater.* 106 (2015) 26–29.
- [63] H. Serier, M. Gaudon, M. Menetrier, Al-doped ZnO powdered materials: al solubility limit and IR absorption properties, *Solid State Sci.* 11 (7) (2009) 1192–1197.
- [64] G.M. Safronov, V.N. Batog, T.V. Stepanyuk, P.M. Fedorov, Equilibrium diagram of the bismuth oxide-zinc oxide system, *Russ. J. Inorg. Chem.* 16 (3) (1971) 460–461.
- [65] L.A. Hughes, K. van Benthem, Effects of electrostatic field strength on grain-boundary core structures in SrTiO₃, *J. Am. Ceram. Soc.* 102 (8) (2019) 4502–4510.
- [66] W. Rheinheimer, J.P. Parras, J.H. Preusker, R.A. De Souza, M.J. Hoffmann, Grain growth in strontium titanate in electric fields: the impact of space-charge on the grain-boundary mobility, *J. Am. Ceram. Soc.* 102 (6) (2019) 3779–3790.
- [67] L.A. Hughes, M. Marple, K. van Benthem, Electrostatic fields control grain boundary structure in SrTiO₃, *Appl. Phys. Lett.* 113 (4) (2018) 041604.
- [68] W. Rheinheimer, X.L. Phuah, H. Wang, F. Lemke, M.J. Hoffmann, H.Y. Wang, The role of point defects and defect gradients in flash sintering of perovskite oxides, *Acta Mater.* 165 (2019) 398–408.
- [69] H.R. Jin, S.H. Yoon, J.H. Lee, N.M. Hwang, D.Y. Kim, J.H. Han, Effect of external electric field on the grain growth of barium titanate in N-2 atmosphere, *J. Mater. Sci. – Mater. Electron.* 16 (11–12) (2005) 749–752.
- [70] H.R. Jin, S.H. Yoon, J.H. Lee, N.M. Hwang, D.Y. Kim, J.H. Han, Effect of external electric field on the grain-growth behavior of barium titanate, *J. Am. Ceram. Soc.* 87 (9) (2004) 1747–1752.
- [71] Y.H. Dong, H.R. Wang, I.W. Chen, Electrical and hydrogen reduction enhances kinetics in doped zirconia and ceria: I. grain growth study, *J. Am. Ceram. Soc.* 100 (3) (2017) 876–886.

- [72] Y. Dong, I.W. Chen, Electrical and hydrogen reduction enhances kinetics in doped zirconia and ceria: II. Mapping electrode polarization and vacancy condensation in ysz, *J. Am. Ceram. Soc.* 101 (3) (2018) 1058–1073.
- [73] R. Raj, Joule heating during flash-sintering, *J. Eur. Ceram. Soc.* 32 (10) (2012) 2293–2301.
- [74] I. Kul'bakin, V. Belousov, S. Fedorov, A. Vorobiev, Solid/melt ZnO-Bi₂O₃ composites as ion transport membranes for oxygen separation from air, *Mater. Lett.* 67 (1) (2012) 139–141.
- [75] V.V. Belousov, Oxygen-permeable membrane materials based on solid or liquid Bi₂O₃, *MRS Commun.* 3 (4) (2013) 225–233.